

Contact algorithms for the material point method in impact and penetration simulation

P. Huang^{1,2}, X. Zhang^{1,3,*}, S. Ma¹ and X. Huang²

¹*AML, School of Aerospace, Tsinghua University, Beijing 100084, People's Republic of China*

²*Institute of Structural Mechanics, China Academy of Engineering Physics, Mianyang 621900, People's Republic of China*

³*State Key Laboratory of Structural Analysis for Industrial Equipment, Dalian University of Technology, Dalian 116023, People's Republic of China*

SUMMARY

The inherent no-slip contact constraint in the standard material point method (MPM) creates a greater penetration resistance. Therefore, the standard MPM was not able to treat the problems involving impact and penetration very well. To overcome these deficiencies, two contact methods for MPM are presented and implemented in our 3D explicit MPM code, MPM3D. In MPM, the impenetrability condition may not be satisfied on the redefined regular grid at the beginning of each time step, even if it has been imposed on the deformed grid at the end of last time step. The impenetrability condition between bodies is only imposed on the deformed grid in the first contact method, while it is imposed both on the deformed grid and redefined regular grid in the second contact method. Furthermore, three methods are proposed for impact and penetration simulation to determine the surface normal vectors that satisfy the collinearity conditions at the contact surface. The contact algorithms are verified by modeling the collision of two elastic rings and sphere rolling problems, and then applied to the simulation of penetration of steel ball and perforation of thick plate with a particle failure model. In the simulation of elastic ring collision, the first contact algorithm introduces significant disturbance into the total energy, but the second contact algorithm can obtain the stable solution by using much larger time step. It seems that both contact algorithms give good results for other problems, such as the sphere rolling and the projectile penetration. Copyright © 2010 John Wiley & Sons, Ltd.

Received 23 May 2009; Revised 11 May 2010; Accepted 2 June 2010

KEY WORDS: material point method; meshfree method; contact; impact; penetration

1. INTRODUCTION

Some physical phenomena arise from the impact and penetration, such as non-linear wave propagation, friction and abrasion, large deformation, dynamic damage and fracture, are usually analyzed by hydrocodes. The broad range of available hydrocodes has been reviewed by Anderson [1] and Benson [2]. Traditionally, the hydrocodes for simulating impact and penetration are developed based on Lagrangian and Eulerian methods. Eulerian methods suffer from the difficulties to treat material interfaces and free interfaces. A boundary layer interface algorithm (BLINT) for sliding interfaces was incorporated into Eulerian CTH hydrocode by Silling [3], and was used to simulate the impact and penetration problems [3, 4].

*Correspondence to: X. Zhang, AML, School of Aerospace, Tsinghua University, Beijing 100084, People's Republic of China.

†E-mail: xzhang@tsinghua.edu.cn

Lagrangian [5, 6] and arbitrary Lagrangian Eulerian methods [7] for the simulation of penetration have been applied extensively in the solid mechanics community. Lagrangian finite element method (FEM) has been used to simulate the penetration based on adaptive meshing, explicit contact/friction algorithm, and rate-dependent plasticity [6]. Although Lagrangian codes have the advantage to track the material interfaces, the distortion and entanglement of mesh often occur in the simulation of penetration. Moreover, a non-physical element erosion algorithm has been often incorporated into Lagrangian codes to model penetration. Recently, the problems involving impact and penetration were solved using some meshless methods, such as Smoothed Particle Hydrodynamics (SPH) [8], Meshless Local Petrov–Galerkin method [9], and Material Point Method (MPM) [10, 11].

MPM developed by Sulsky *et al.* [10, 11] is an extension of the particle-in-cell method [12, 13] to solid mechanics problems. Being a fully Lagrangian particle method, it discretizes a material domain by using a collection of material points. The momentum equations are solved on a predefined regular background grid, so that the grid distortion and entanglement are completely avoided. MPM has been applied to solve many complicated engineering problems, such as the upsetting process [14], Taylor bar impact [15], dynamics crack [16, 17], explosive process [18, 19], hypervelocity impact [20, 21] and dynamic analysis of saturated porous media [22]. Although MPM has been successfully applied to solve hypervelocity problems, the MPM simulations for penetration problems are still challenging tasks.

Because of using the single-valued mapping functions between background grid nodes and particles, interpenetration of material particles is precluded in the standard MPM algorithm. A no-slip contact constraint is inherent in the standard MPM. Sulsky *et al.* [11] performed a standard MPM simulation for a steel sphere impacting an aluminum target at a striking velocity of 1160 m/s. They found that the penetration depth computed by the standard MPM is significantly lower than the experimental result. Hence, in some problems involving impact and penetration, the inherent no-slip contact condition in the standard MPM may create a greater penetration resistance, and an efficient contact algorithm for releasing no-slip contact should be developed.

A simple contact algorithm was proposed by York *et al.* [23] to allow the release of no-slip contact constraint in the standard MPM. In York's method, if the bodies are coming into contact with each other, the standard MPM method is used to impose the impenetrability condition. If the bodies are moving away from one another, they move in their own velocity fields to allow separation. To avoid interpenetration and allow separation in the gear contact process, Hu and Chen [24] presented a contact/sliding/separation algorithm in the multi-mesh environment. In their contact algorithm, the normal velocity of each material particle at the contact surface is calculated in the common background grid, whereas the tangential velocity is found based on the respective individual grid. Although aforementioned contact algorithms are efficient to separation, the friction between contact bodies is not considered.

Bardenhagen *et al.* [25, 26] proposed a contact/friction/separation algorithm in multi-velocity fields. The impenetrability condition and Coulomb friction between bodies are incorporated into MPM when the contact occurs. The contact force between bodies is obtained from the relative nodal velocity at the contact surface. The approach has been demonstrated using the sphere rolling on an inclined plane and the granular shearing simulation [26]. Recently, Pan *et al.* [27] proposed a three-dimensional multi-mesh contact algorithm for MPM. In this contact algorithm, the contact force between bodies is obtained from the normal nodal acceleration continuity requirement at the contact surface. The approach presented by Pan *et al.* [27] was applied to simulate the collision of plastic spheres and the impact of Taylor bar. The problems involving penetration are more complicated than the common contact problems, so that the contact MPM algorithms for penetration simulation are needed to be developed.

The contact conditions in MPM are applied via the background grid, and the contact problems can be completely described by the nodal variables. In this paper, a general formulation of the contact-impact problem is first presented, and then two methods are presented to implement the contact algorithm in the well-known Lagrange multiplier form. The impenetrability condition is only imposed on the deformed grid at the end of each time step in the first method, whereas it is

imposed both on the deformed grid at the end of each time step and the redefined regular grid at the beginning of next time step in the second method. With a particle failure model, two contact methods are applied to simulate the penetration of steel ball and perforation of thick plate.

This paper is organized as follows. The basic mathematical descriptions of the contact problem are summarized in Section 2. Two contact methods for MPM are presented in details in Section 3, and their implementations are described in Section 4. In Section 5, the problems involving impact and penetration are solved by the presented contact methods, and the computational results are compared with the experimental results. Finally, some conclusions are presented in Section 6.

2. BASIC DESCRIPTIONS OF CONTACT PROBLEMS

In MPM, each body is discretized by a set of particles, which carry all state variables such as stress, strain and temperature. The MPM algorithm also uses a background grid. Figure 1 shows an example of the discrete representation of a two-dimensional material body. Particles are assigned fixed masses during computation, so that conservation of mass is satisfied implicitly in MPM. The momentum equations are solved on the background grid. The momentum changes on the grid are interpolated to the particles, so that the total momentum is conserved in MPM. Energy conservation errors are dependent on the time step in explicit MPM [28].

Narin [29] compared three numerical schemes of MPM, which are update stress last [10], modified update stress last [30] and update stress first (USF) [28, 31] schemes. The USF scheme is similar to the numerical scheme used in explicit FEM, and it is used in this study.

2.1. Contact condition

Consider two continuous bodies (body I and body II) which come into contact with each other at time t^k . The algorithm can be developed to treat the contact behaviors of any number of bodies, but we restrict two bodies for simplicity of notation. Let the subscript i denote the value of grid node i , and let the subscript p denote the value of particle p . Let the superscripts k and $k+1$ denote the value at time t^k and t^{k+1} , respectively. Δt is the current time increment, $\Delta t = t^{k+1} - t^k$, S_{ip} and G_{ip} are the shape function and its gradient of node i evaluated at particle p , respectively.

In the contact algorithm [25], the mass and momentum from material points are interpolated to the computational grid for each individual body, respectively. The contact conditions are applied by the background grid in MPM. According to the principles of continuum mechanics, the contact conditions can be described as follows [32, 33]:

2.1.1. Impenetrability condition. Once the contact occurs between two bodies at time t^k , the outward unit normal vectors of two bodies must be in the opposite direction at the contact surface,

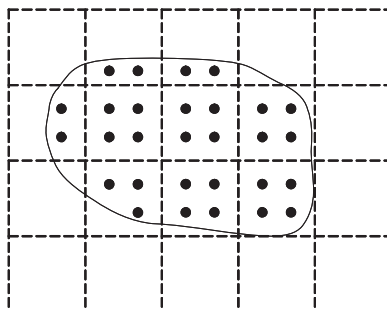


Figure 1. Material discretization in MPM.

namely

$$\sum_{b=1}^2 \mathbf{n}_{bi} = 0 \quad (1)$$

where b indexes the bodies, \mathbf{n}_{bi} is the outward unit normal vector of the body surface. The nodal velocity must satisfy the impenetrability condition on the background grid, that is

$$\sum_{b=1}^2 \mathbf{v}_{bi} \cdot \mathbf{n}_{bi} = 0 \quad (2)$$

where \mathbf{v}_{bi} is the nodal velocity of node i connecting to body b .

2.1.2. Contact force condition. The contact force $\mathbf{f}_{bi}^{\text{ct}}$ is applied to body b when the contact occurs. Based on Newton's third law, the contact force yields

$$\sum_{b=1}^2 \mathbf{f}_{bi}^{\text{ct}} = 0 \quad (3)$$

The normal contact force f_i^{nor} of two bodies is defined by:

$$f_i^{\text{nor}} = \mathbf{f}_{bi}^{\text{ct}} \cdot \mathbf{n}_{bi} \quad \text{and} \quad f_i^{\text{nor}} \leq 0 \quad (4)$$

The normal contact force f_i^{nor} must be less than or equal to zero because the normal contact force cannot be tensile.

2.1.3. Momentum equations. The weak form of the contact problem is obtained from the principle of virtual work by appending the Lagrange multiplier term. After imposing the contact constraints by using the Lagrange multiplier method, the momentum equations of grid nodes at the contact surface can be written as

$$m_{bi} \mathbf{a}_{bi} = \mathbf{f}_{bi} + \mathbf{f}_{bi}^{\text{ct}} \quad (b = 1, 2) \quad (5)$$

where m_{bi} is the nodal mass, \mathbf{a}_{bi} is the nodal acceleration, \mathbf{f}_{bi} is the sum of the nodal internal and external forces, and $\mathbf{f}_{bi}^{\text{ct}}$ is the nodal contact force.

2.2. Detection of contact nodes

For each body, the nodal velocity connecting to body b is computed by taking the ratio of momentum \mathbf{p}_{bi} to mass m_{bi}

$$\mathbf{v}_{bi} = \frac{\mathbf{p}_{bi}}{m_{bi}} \quad (b = 1, 2) \quad (6)$$

If the velocities of two bodies are projected on to the same node, the contact may occur. The average mapping velocity of all material points in grid node i is termed the centre-of-mass velocity and denoted \mathbf{v}_i^{cm}

$$\mathbf{v}_i^{\text{cm}} = \frac{\mathbf{p}_{1i} + \mathbf{p}_{2i}}{m_{1i} + m_{2i}} \quad (7)$$

Using the surface normal vector, approach and departure of contact bodies can be distinguished. A body is coming into contact with its neighbor body in the vicinity of grid node i when

$$(\mathbf{v}_{bi} - \mathbf{v}_i^{\text{cm}}) \cdot \mathbf{n}_{bi} > 0 \quad (8)$$

If the nodal mass m_{bi} is close to zero, the nodal velocity \mathbf{v}_{bi} maybe become a singular value which causes error during the calculation. A more accurate solution in MPM is obtained using the nodal momentum rather than the nodal velocity [11].

2.3. Surface normal vectors

The gradient of the nodal mass m_{bi} in the individual body provides an original computation of the unit surface normal vector [26]. Hence,

$$\hat{\mathbf{n}}_{bi} = \frac{1}{\left| \sum_p \mathbf{G}_{ip} m_{bp} \right|} \sum_p \mathbf{G}_{ip} m_{bp} \quad (b=1, 2) \quad (9)$$

where m_{bp} is the mass of particle p in body b .

The normal vectors given by Equation (9) cannot guarantee that the collinearity condition Equation (1) will be satisfied at the contact surface. Non-collinearity of normal vectors at contact surface causes non-conservation of momentum in contact algorithms. Following methods are proposed to determine the modified surface normal vectors \mathbf{n}_{bi} which satisfies the collinearity condition equation (1) at the contact surface.

1. If body I is stiffer than body II, let $\mathbf{n}_{1i} = \hat{\mathbf{n}}_{1i}$ and $\mathbf{n}_{2i} = -\hat{\mathbf{n}}_{1i}$.
2. If body I with a flat/convex surface is expected to come into contact with body II with a concave surface, let $\mathbf{n}_{1i} = \hat{\mathbf{n}}_{1i}$ and $\mathbf{n}_{2i} = -\hat{\mathbf{n}}_{1i}$.
3. The modified normal vector $\mathbf{n}_{bi}(b=1, 2)$ can also be obtained by the average value of original normal vectors, e.g.

$$\mathbf{n}_{1i} = -\mathbf{n}_{2i} = \frac{1}{|\hat{\mathbf{n}}_{1i} - \hat{\mathbf{n}}_{2i}|} (\hat{\mathbf{n}}_{1i} - \hat{\mathbf{n}}_{2i}) \quad (10)$$

The modified normal vector \mathbf{n}_{bi} satisfies the collinearity condition equation (1) at contact surface, which insures the momentum conservation in the contact computation.

3. CONTACT ALGORITHMS

Contact-impact algorithms are implemented with the explicit time integration method. In MPM, the deformed grid at the end of each time step is discarded, and a new regular background grid is redefined at the beginning of next time step. Consequently, the impenetrability condition equation (2) may not be satisfied on the redefined regular grid at the beginning of each time step, even if it has been imposed on the deformed grid at the end of last time step. Two methods are presented here to implement the contact algorithm. The impenetrability condition equation (2) is only imposed on the deformed grid in the first method, whereas it is imposed both on the deformed grid and the redefined regular grid in the second method.

At the beginning of each time step, the contact between two bodies may occur at a node if the velocities of both bodies are projected to the node. The contact algorithm is required to impose the impenetrability condition equation (2) at the contact node.

3.1. The first contact method

In the first method, the contact conditions are imposed after the two bodies have been updated in an uncoupled manner [34, 35]. In each time step, the bodies are first integrated independently to obtain the trial values of nodal variables, as if they were not in contact.

Integrating the momentum equation of bodies independently gives the trial nodal velocity $\bar{\mathbf{v}}_{bi}^{k+1}$ at time t^{k+1}

$$\bar{\mathbf{v}}_{bi}^{k+1} = \mathbf{v}_{bi}^k + \frac{\mathbf{f}_{bi}}{m_{bi}^k} \Delta t \quad (11)$$

At the end of the time step, a body may penetrate its neighbor body in the vicinity of grid node i when

$$(\bar{\mathbf{v}}_{bi}^{k+1} - \bar{\mathbf{v}}_i^{\text{cm}, k+1}) \cdot \mathbf{n}_{bi}^k > 0 \quad (12)$$

holds, and the trial values of nodal velocities should be corrected to new values so that the impenetrability condition equation (2) is satisfied. Otherwise, the trial values of nodal velocities represent the true solution. In Equation (12), $\bar{\mathbf{v}}_i^{\text{cm},k+1}$ is the center-of-mass velocity based on the trial nodal velocity. That is

$$\bar{\mathbf{v}}_i^{\text{cm},k+1} = \frac{m_{1i}^k \bar{\mathbf{v}}_{1i}^{k+1} + m_{2i}^k \bar{\mathbf{v}}_{2i}^{k+1}}{m_{1i}^k + m_{2i}^k} \quad (13)$$

This uncoupled solution correctly indicates which parts of the body are in contact at the end of time step; hence, no iterations are needed to establish the contact interface.

For bodies in contact, the corrected nodal velocity at time t^{k+1} is given by

$$\mathbf{v}_{bi}^{k+1} = \bar{\mathbf{v}}_{bi}^{k+1} + \frac{\mathbf{f}_{bi}^{\text{ct}}}{m_{bi}^k} \Delta t \quad (14)$$

which must satisfy the impenetrability condition

$$\sum_{b=1}^2 \mathbf{v}_{bi}^{k+1} \cdot \mathbf{n}_{bi}^k = 0 \quad (15)$$

Substituting Equation (14) into Equation (15) gives the normal contact force

$$\mathbf{f}_i^{\text{nor}} = \mathbf{f}_{bi}^{\text{ct}} \cdot \mathbf{n}_{bi}^k = \frac{m_{1i}^k m_{2i}^k}{(m_{1i}^k + m_{2i}^k) \Delta t} (\bar{\mathbf{v}}_{2i}^{k+1} - \bar{\mathbf{v}}_{1i}^{k+1}) \cdot \mathbf{n}_{1i}^k \quad (16)$$

Substituting Equation (13) into (16) leads to the following simplified form:

$$\mathbf{f}_i^{\text{nor}} = \frac{m_{bi}^k}{\Delta t} (\bar{\mathbf{v}}_i^{\text{cm},k+1} - \bar{\mathbf{v}}_{bi}^{k+1}) \cdot \mathbf{n}_{bi}^k \quad (17)$$

The contact algorithm has been finished if there is no friction between bodies. The tangential contact force, or friction, can be determined according to the similar procedure to the normal contact force computation. We first calculate the tangential force necessary to cause two bodies to stick completely. The tangential component of the contact force for no-slip contact is defined by

$$\mathbf{f}_i^{\text{tan}} = \mathbf{f}_{bi}^{\text{ct}} \cdot \mathbf{s}_{bi}^k \quad (18)$$

where $\mathbf{f}_{bi}^{\text{ct}}$ is the contact force applied to body b , \mathbf{s}_{bi}^k is the unit tangential vector, which satisfies $\mathbf{s}_{1i}^k = -\mathbf{s}_{2i}^k$ at the contact surface.

For no-slip contact, \mathbf{v}_{bi}^{k+1} must satisfy

$$\sum_{b=1}^2 \mathbf{v}_{bi}^{k+1} \cdot \mathbf{s}_{bi}^k = 0 \quad (19)$$

Substituting Equations (14) into Equation (19) and adopting Equation (13), the tangential component of the contact force for no-slip contact is given by:

$$\begin{aligned} \mathbf{f}_i^{\text{tan}} &= \frac{m_{1i}^k m_{2i}^k}{(m_{1i}^k + m_{2i}^k) \Delta t} (\bar{\mathbf{v}}_{2i}^{k+1} - \bar{\mathbf{v}}_{1i}^{k+1}) \cdot \mathbf{s}_{1i}^k \\ &= \frac{m_{bi}^k}{\Delta t} (\bar{\mathbf{v}}_i^{\text{cm},k+1} - \bar{\mathbf{v}}_{bi}^{k+1}) \cdot \mathbf{s}_{bi}^k \end{aligned} \quad (20)$$

The tangential force of non-slip contact can also be obtained by:

$$\mathbf{f}_i^{\text{tan}} \mathbf{s}_{bi}^k = \frac{m_{bi}^k}{\Delta t} (\bar{\mathbf{v}}_i^{\text{cm},k+1} - \bar{\mathbf{v}}_{bi}^{k+1}) - \mathbf{f}_i^{\text{nor}} \mathbf{n}_{bi}^k \quad (21)$$

For slip contact, the friction at the contact surface is described by the Coulomb friction model. We limit the frictional force to have a magnitude less than the tangential contact force of no-slip contact so that the contact force is obtained as:

$$f_{bi}^{ct} = \min(0, f_i^{nor})n_{bi}^k + \min(\mu|f_i^{nor}|, |f_i^{tan}|)s_{bi}^k \tag{22}$$

After calculating the contact force f_{bi}^{ct} from Equation (22), the corrected nodal velocity v_{bi}^{k+1} at time t^{k+1} can be obtained from Equation (14).

3.2. The second contact method

In FEM, the same Lagrangian meshes are used in all time steps. Hence, the impenetrability condition equation (2) will be still satisfied at the beginning of each time step if it is imposed at the end of last time step. However, in MPM, the deformed background grid is discarded at the end of each time step, and a new regular background grid is redefined at the beginning of next time step. The impenetrability condition Equation (2) may be not satisfied at the beginning of each time step, even if it has been imposed at the end of last time step.

In the second method, the impenetrability condition is forced to be satisfied both at the end of each time step and at the beginning of the next time step. At the beginning of each time step, if the velocities of two bodies are projected to the same node, and the initial nodal velocities v_{bi}^k satisfy the condition

$$(v_{bi}^k - v_i^{cm,k}) \cdot n_{bi}^k > 0 \tag{23}$$

The impenetrability condition equation (2) is not satisfied, and the nodal velocities v_{bi}^k should be adjusted to new values \tilde{v}_{bi}^k so that the condition

$$\tilde{v}_{bi}^k \cdot n_{bi}^k = v_i^{cm,k} \cdot n_{bi}^k \tag{24}$$

holds. In Equations (23) and (24), $v_i^{cm,k}$ is the center-of-mass velocity based on the initial nodal velocity.

Equation (24) indicates that the normal component of the adjusted nodal velocities is set equal to the normal component of the center-of-mass velocity. That is

$$\tilde{v}_{bi}^k = \begin{cases} v_{bi}^k - [(v_{bi}^k - v_i^{cm,k}) \cdot n_{bi}^k]n_{bi}^k & \text{slip contact} \\ v_i^{cm,k} & \text{no-slip contact} \end{cases} \tag{25}$$

The trial nodal velocity \tilde{v}_{bi}^{k+1} at time t^{k+1} is obtained by integrating the momentum equation of each body independently as:

$$\tilde{v}_{bi}^{k+1} = \tilde{v}_{bi}^k + \frac{f_{bi}}{m_{bi}^k} \Delta t \tag{26}$$

The remaining steps of the second method are the exactly same as that of the first method.

Note that the stresses on particles are updated based on the nodal velocities at the beginning of each time step in USF scheme. Therefore, the nodal velocities, v_{bi}^k , used to update the stresses in the first contact method may violate the impenetrability condition Equation (2). Violating the impenetrability condition in updating stresses may leads disturbances to the system, which has been observed in the numerical results presented in Section 5.

4. IMPLEMENTATION OF THE CONTACT ALGORITHMS

The detailed implementation of two contact methods are presented here using USF scheme for one time step. The beginning of the current time step is t^k , and the end of the current time step is t^{k+1} .

1. Redefine the background grid at the beginning of the current time step. Compute the nodal mass m_{bi}^k

$$m_{bi}^k = \sum_p m_{bp} S_{ip}^k \quad (27)$$

the nodal velocity \mathbf{v}_{bi}^k

$$m_{bi}^k \mathbf{v}_{bi}^k = \sum_p m_{bp} \mathbf{v}_{bp}^k S_{ip}^k \quad (28)$$

and the normal vector \mathbf{n}_{bi}^k connecting to body b .

2. Detect the contact nodes. If the velocities \mathbf{v}_{bi}^k of two bodies are projected to the same node, two bodies contact at the node.
3. For the second method, adjust the nodal velocities \mathbf{v}_{bi}^k of contact nodes to new values $\tilde{\mathbf{v}}_{bi}^k$ according to Equation (25) if the velocities \mathbf{v}_{bi}^k of two bodies satisfy the condition Equation (23).
4. Compute the strain increments $\Delta \boldsymbol{\varepsilon}_{bp}$ of particles from the nodal velocities \mathbf{v}_{bi}^k (or $\tilde{\mathbf{v}}_{bi}^k$ in the second method) connecting to each body, and update the particle stress $\boldsymbol{\sigma}_{bp}^{k+1}$ using a constitutive model. Update the particle density ρ_{bp}^{k+1} .
The strain increment of each particle can be evaluated by

$$\Delta \boldsymbol{\varepsilon}_{bp} = \frac{\Delta t}{2} \sum_{i=1}^8 [\mathbf{G}_{ip}^k \mathbf{v}_{bi}^k + (\mathbf{G}_{ip}^k \mathbf{v}_{bi}^k)^T] \quad (29)$$

where $\mathbf{G}_{ip}^k = \nabla N_i |_{\mathbf{x}=\mathbf{x}_p^k}$.

The density of a particle is updated by:

$$\rho_{bp}^{k+1} = \frac{\rho_{bp}^k}{1 + \text{tr}(\Delta \boldsymbol{\varepsilon}_{bp})} \quad (30)$$

5. Compute the nodal force \mathbf{f}_{bi} from the updated stresses of particles belonging to body b by

$$\mathbf{f}_{bi} = - \sum_p \mathbf{G}_{ip}^k \cdot \boldsymbol{\sigma}_{bp}^{k+1} \frac{m_{bp}}{\rho_{bp}^{k+1}} + \mathbf{f}_{bi}^{\text{ext}} \quad (31)$$

where

$$\mathbf{f}_{bi}^{\text{ext}} = \sum_p m_{bp} S_{ip}^k \mathbf{b}_{bp}^k + \int_{\Gamma_t} S_i^k \mathbf{t}_b^k d\Gamma \quad (32)$$

is the external force of grid node i , \mathbf{b} is the specific body force, and \mathbf{t} is the prescribed traction on boundary Γ_t .

6. Compute the trial nodal velocity $\tilde{\mathbf{v}}_{bi}^{k+1}$ from Equation (11) (or from Equation (26) in the second method) by integrating the momentum equation of each body independently.
7. Loop over all grid nodes. Calculate the contact forces $\mathbf{f}_{bi}^{\text{ct}}$ from Equation (22) for contact nodes if the trial nodal velocity satisfies Equation (12).
8. If two bodies are in contact at node i , compute the final nodal velocity \mathbf{v}_{bi}^{k+1} at time t^{k+1} from Equation (14). Otherwise, the trial solution represents the true solution, namely $\mathbf{v}_{bi}^{k+1} = \tilde{\mathbf{v}}_{bi}^{k+1}$.
9. For each body, update the particle position and velocity. The position of particle p belonging to body b is updated by

$$\mathbf{x}_{bp}^{k+1} = \mathbf{x}_{bp}^k + \Delta t \sum_{i=1}^8 \mathbf{v}_{bi}^{k+1} S_{ip}^k \quad (33)$$

and the velocity of particle p belonging to body b is updated by:

$$\mathbf{v}_{bp}^{k+1} = \mathbf{v}_{bp}^k + \Delta t \sum_{i=1}^8 \frac{\mathbf{f}_{bi} + \mathbf{f}_{bi}^{\text{ct}}}{m_{bi}^k} S_{ip}^k \quad (34)$$

The explicit time integration is used in the contact algorithms of MPM, hence the Courant stability restriction is applied to the time step to ensure numerical stability. The time step size is calculated from

$$\Delta t_{cr} = \alpha \Delta x / c_p \quad (35)$$

where α is the time step scale factor, Δx is the cell length, c_p is the wave speed.

5. APPLICATIONS

The contact algorithms presented in this paper have been implemented in our explicit 3D MPM code, MPM3D. Collision of two elastic rings and sphere rolling is first simulated using MPM3D to investigate the accuracy of two contact methods. Then, the penetration of steel ball and the perforation of thick plate are solved, and numerical results are compared with the experimental results.

5.1. Collision of two elastic rings

The collision of elastic rings is simulated for verifying our contact algorithms and code. This problem has been used to study the tensile instability and unphysical fracture in SPH [36, 37]. The large deformation provides a challenging test of code, and these rings should bounce off each other without disintegration. The inner and outer radii of the ring are 30 and 40 mm, respectively. Both of rings are simulated as compressible Neo-Hookean material models with a bulk modulus of 121.7 MPa, a shear modulus of 26.1 MPa and a density of 1.01 g/cm³. The rings are launched with a speed of 30 m/s so that the relative speed is 60 m/s. The frictional coefficient between the elastic rings is set to 0.1. In this simulation, the grid is uniform with equal spacing in all directions and eight material points per cell. The initial particle space is 1 mm, and the cell size is set equal to 2 mm. Each ring includes 29 760 particles.

Figures 2 and 3 compare the configurations at various time steps obtained by the first contact method and the second contact method, respectively, where the time step scale factor $\alpha=0.25$. In these figures, (a) shows the initial configuration, and the following frames show subsequent impact and rebound. Figures 2 and 3 show that the contact surface obtained from the second contact method is better than that obtained from the first method. Therefore, the accuracy of the second contact method is higher than that of the first contact method. In Figures 2 and 3, the stress wave propagation pattern is shown to illustrate the collision process.

Figure 4 plots the time history of total energy with different time step scale factors. Compared with the first contact method, the second contact method can obtain a stable solution with a much larger time step scale factor. As aforementioned, violating the impenetrability condition in updating stresses in the first contact method may introduce disturbance into the system. This has been clearly shown in Figure 4(a), in which many steep steps have been observed in the time history of the total energy before the separation of two rings at time $t=3.4$ ms.

5.2. Sphere rolling simulation

An elastic sphere on an inclined elastic plane [26] as shown in Figure 5(a) is simulated. The sphere will roll and slip when $\tan \theta > 3.5 \mu$, otherwise, the sphere will roll and stick. For an initial stationary rigid sphere on an inclined rigid surface, the x -component of the center-of-mass position $x_{cm}(t)$ is given by

$$x_{cm}(t) = \begin{cases} x_0 + \frac{1}{2} g t^2 (\sin \theta - \mu \cos \theta), & \tan \theta > 3.5 \mu \quad (\text{slip}) \\ x_0 + \frac{5}{14} g t^2 \sin \theta, & \tan \theta \leq 3.5 \mu \quad (\text{stick}) \end{cases} \quad (36)$$

where x_0 is the x -component of the initial center-of-mass position, and g is the magnitude of the gravity acceleration.

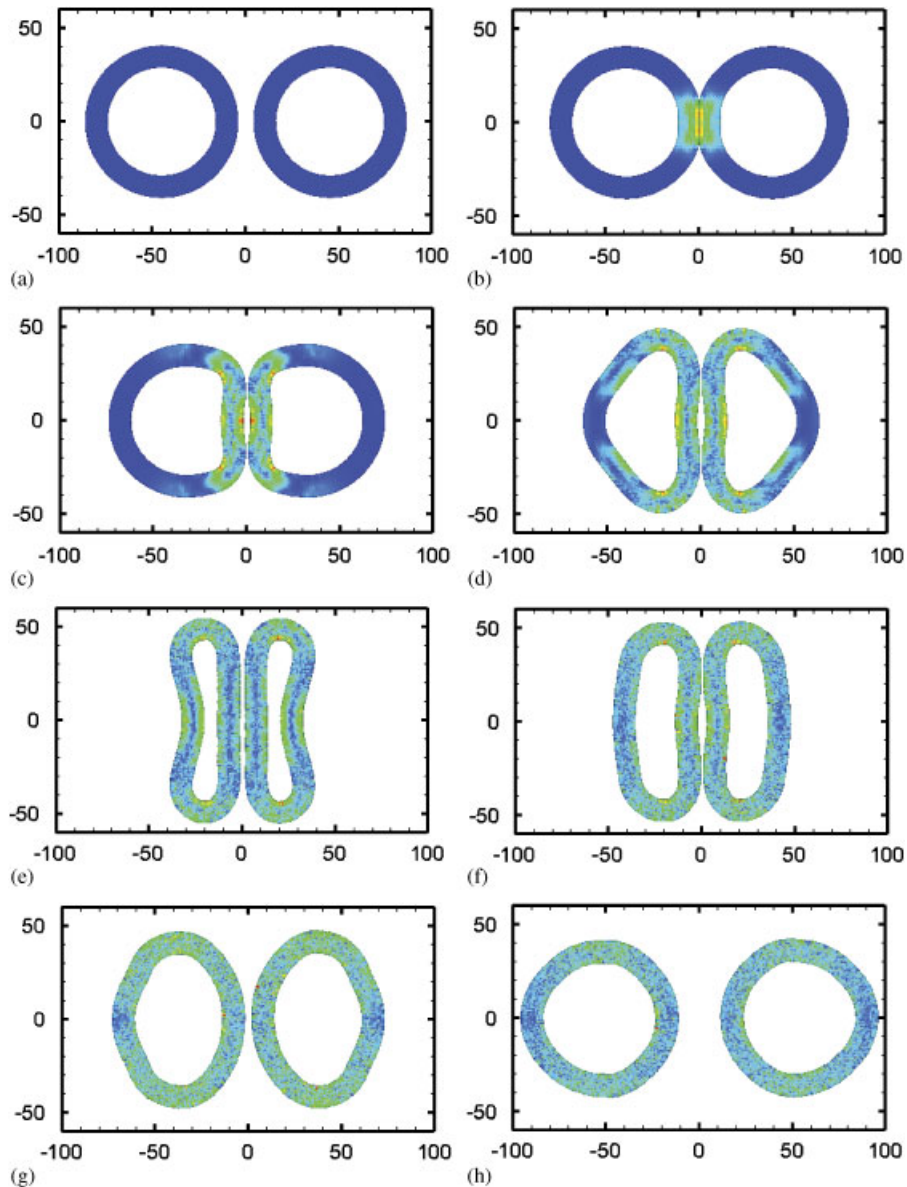


Figure 2. Configurations of elastic rings at various time steps obtained by the first contact method ($\alpha=0.25$): (a) $t=0$ ms; (b) $t=0.2$ ms; (c) $t=0.4$ ms; (d) $t=0.8$ ms; (e) $t=1.8$ ms; (f) $t=2.8$ ms; (g) $t=3.8$ ms; and (h) $t=4.8$ ms.

In this simulation, the radius of sphere is $R=1.6$ m, the dimensions of plane are a length of 20 m, a width of 4.0 m and a thickness of 0.8 m. The magnitude of gravity acceleration is taken to be 10 m/s^2 . The sphere has a bulk modulus of 7 MPa, a shear modulus of 1.5 MPa and a density of 1 g/cm^3 . The plane has bulk modulus 70 MPa, shear modulus 15 MPa and density 10 g/cm^3 . Both the materials have same wave speed 95 m/s. The bottom of plane is fixed in the simulations. The grid is uniform with equal spacing in all directions and eight material points per cell. The initial maximum particle space is 0.1 m, and the cell size is set equal to 0.2 m. The sphere is discretized by 49 560 particles, whereas the plane by 64 000 particles, as shown in Figure 5(b).

Two cases are analyzed. In the first case, the inclined angle is $\theta=\pi/4$ and the frictional coefficient is $\mu=0.4$, so that the sphere will roll and stick, whereas in the second case, the inclined angle

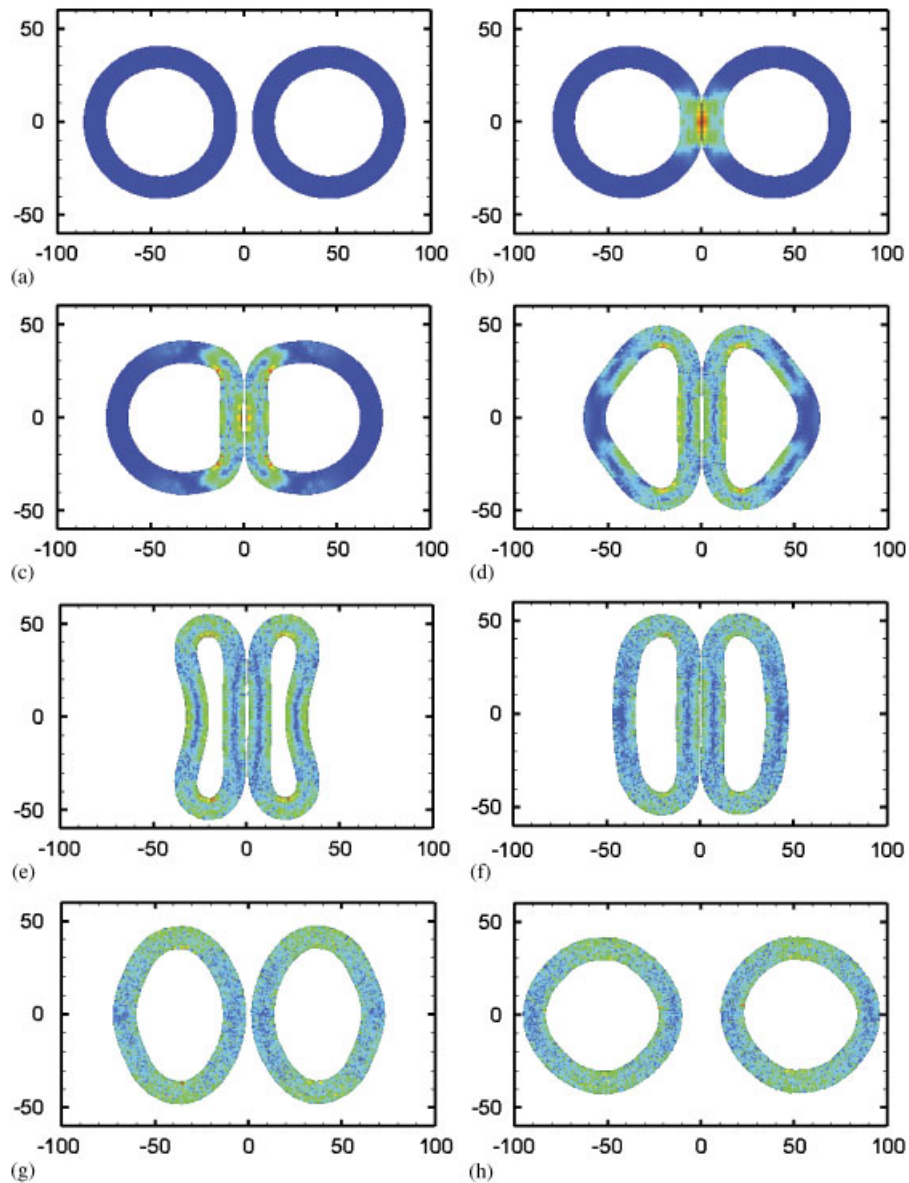


Figure 3. Configurations of elastic rings at various time steps obtained by the second contact method ($\alpha=0.25$): (a) $t=0$ ms; (b) $t=0.2$ ms; (c) $t=0.4$ ms; (d) $t=0.8$ ms; (e) $t=1.8$ ms; (f) $t=2.8$ ms; (g) $t=3.8$ ms; and (h) $t=4.8$ ms.

is $\theta=\pi/3$ and the frictional coefficient is $\mu=0.2$ so that the sphere will roll and slip. Figure 6 compares the numerical results of the center-of-mass position of sphere obtained by two contact methods with the analytical solutions of rigid sphere.

The analytic solutions of rigid sphere give an upper bound of the x -component of the center-of-mass position for these computations. The potential energy is converted both to strain energy and to kinetic energy in the simulations due to the elasticity of sphere and surface, whereas the potential energy is only converted to kinetic energy in the analytic solutions. Figure 6 shows that both contact methods give sufficient accuracy solutions for both slip and stick cases in this simulation.

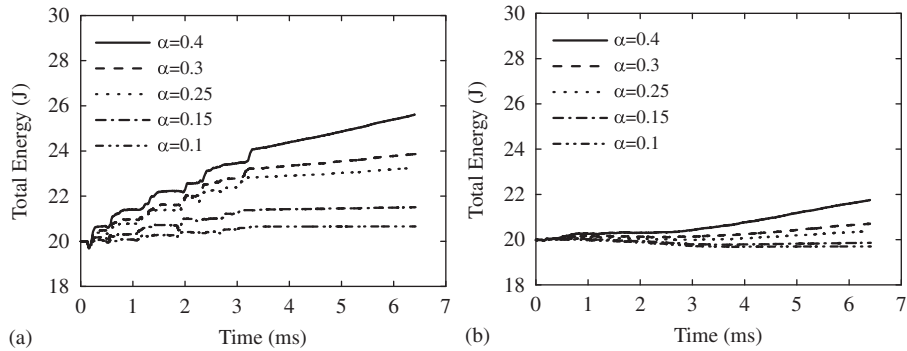


Figure 4. Time history of total energy with different time step scale factors obtained by: (a) the first contact method and (b) the second contact method.

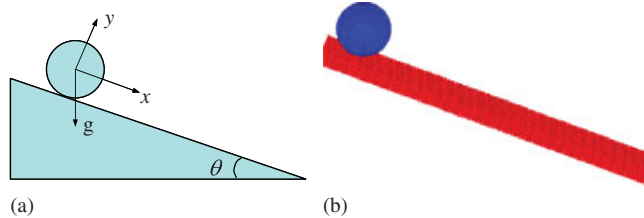


Figure 5. Geometry and MPM models for simulation of a sphere on an inclined plane: (a) geometry configuration and (b) MPM model.

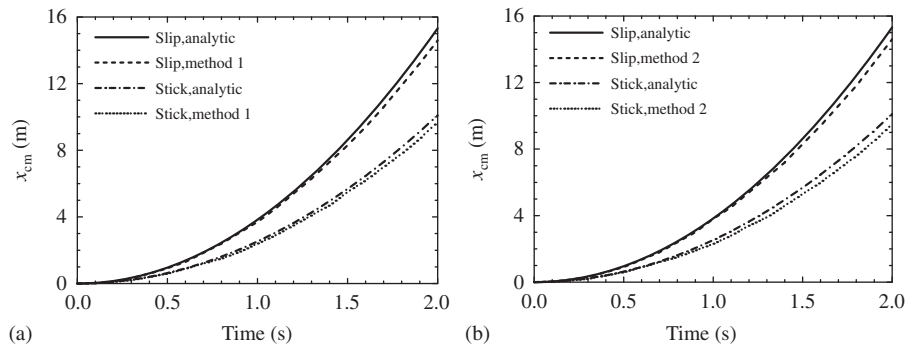


Figure 6. Time history of sphere center-of-mass x -position for both the slip and stick cases obtained by: (a) the first contact method and (b) the second contact method.

5.3. Penetration of steel ball

A steel ball with a diameter of 10 mm impacting a thin circular steel plate with a thickness of 1 mm and a diameter of 178 mm is simulated using MPM3D with the contact algorithms. The impact speed of the steel ball is 200 m/s and the direction of impact is normal to the target plate.

In the simulations, the deviatoric stress is updated by the elastic–plastic constitutive model with isotropic hardening

$$\sigma_y = A + B\bar{\epsilon}_p^n \quad (37)$$

where A , B and n are the material constants, σ_y is the flow stress and $\bar{\epsilon}_p$ is the effective plastic strain. The pressure p is updated by the Mie-Grüneisen equation of state

$$p = \begin{cases} \frac{\rho c_0^2 \mu (1 + \mu)}{[1 - (s-1)\mu]^2} \left(1 - \frac{\gamma \mu}{2}\right) + \gamma_0 E_n, & \mu > 0 \\ \rho c_0^2 \mu + \gamma_0 E_n, & \mu < 0 \end{cases} \quad (38)$$

where ρ , c_0 , s and γ_0 are the material constants, μ is the compression ratio of relative volume, γ is the Grüneisen coefficient and E_n is the internal energy per initial volume. The material constants of the steel are taken from Reference [38], and listed in Table I. According to De Vuyst [39] and Wingate [40], the particle failure is taken into account by setting the deviatoric components of the stress tensor to zero when the effective plastic strain reaches the failure strain. The failure strain ϵ_{fail} for steel is set equal to 0.57.

One-fourth of the model is considered in the calculation due to symmetry. The projectile and the target are discretized by 33 664 particles and 398 184 particles, respectively. The grid is uniform with a cell size of 0.5 mm and eight particles per cell. The initial particle space is 0.25 mm.

This problem is solved by the standard MPM and the proposed contact methods, respectively. The time step scale factor $\alpha = 0.4$, and the frictional coefficient μ between the projectile and target is set to zero. The configurations with equivalent plastic strain obtained by different algorithms are illustrated in Figures 7, 8 and 9, respectively.

As shown in Figure 7, the inherent no-slip contact condition in the standard MPM creates a greater penetration resistance so that the target has not been perforated by the projectile, which does not agree with the experiment results [38]. In contrast, the target is perforated by the projectile in the two contact simulations, as shown in Figures 8 and 9, respectively. The projectile's residual velocities V_r obtained from the two contact methods are 89.4 and 85.8 m/s, respectively.

Table I. Material constants of steel.

ρ (kg/m ³)	E (GPa)	ν	A (MPa)	B (MPa)	n	c_0 (m/s)	s	γ_0	ϵ_{fail}
7850	200.0	0.30	600.0	275.0	0.36	3600	1.90	1.70	0.57

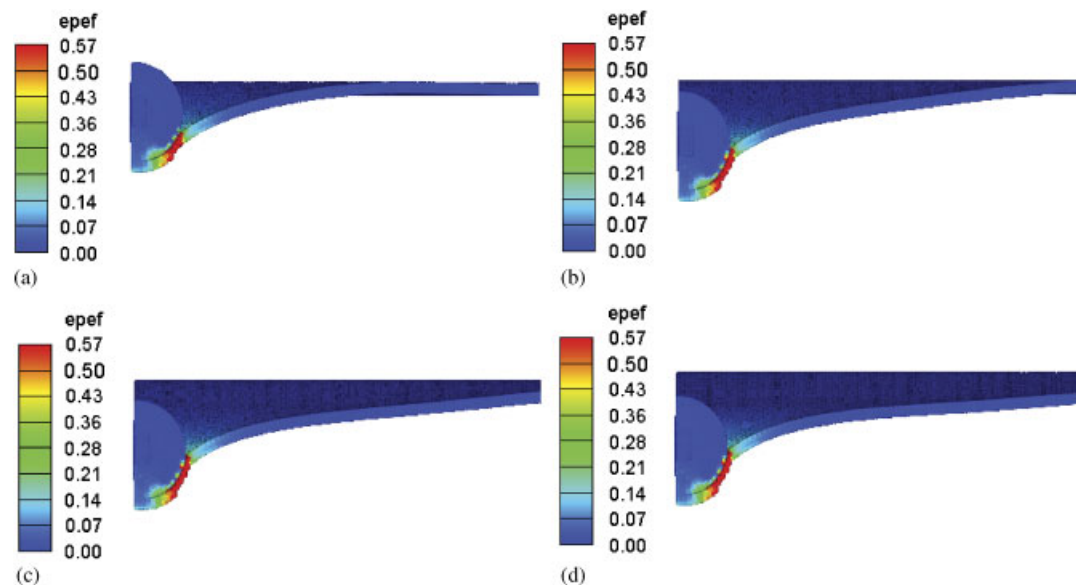


Figure 7. The configurations at various time steps obtained by the standard MPM, where $epef$ represents the equivalent plastic strain. The target is not perforated by the projectile: (a) $t = 60 \mu\text{s}$; (b) $t = 120 \mu\text{s}$; (c) $t = 180 \mu\text{s}$; and (d) $t = 240 \mu\text{s}$.

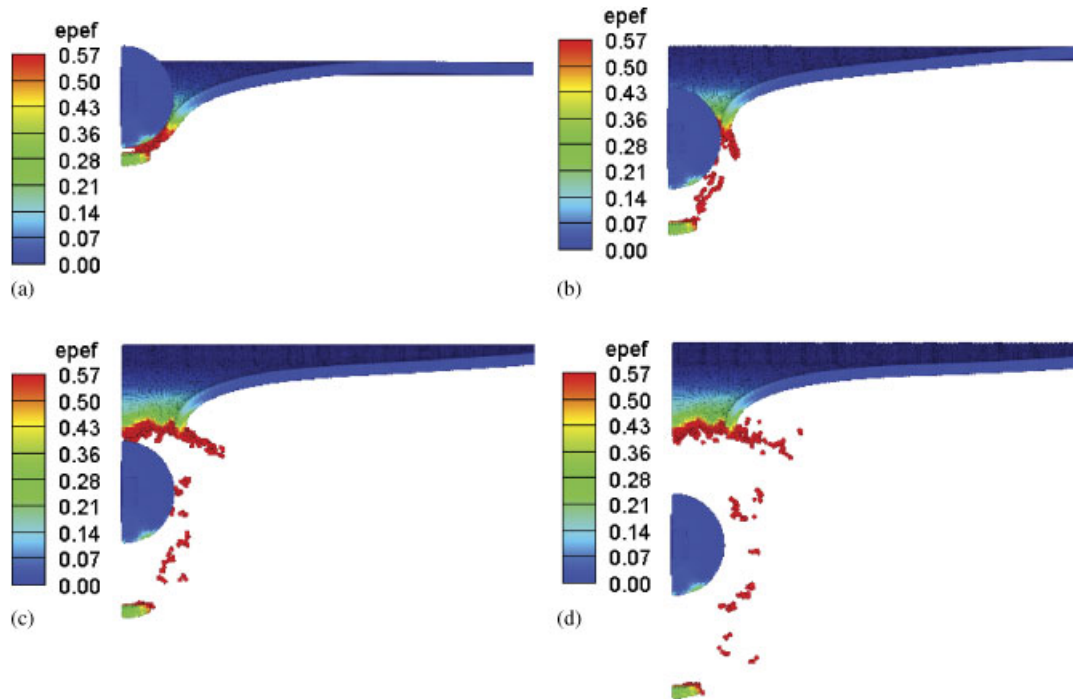


Figure 8. The configurations at various time step obtained by the first contact method, where epef represents the equivalent plastic strain. $V_t = 89.4 \text{ m/s}$: (a) $t = 60 \mu\text{s}$; (b) $t = 120 \mu\text{s}$; (c) $t = 180 \mu\text{s}$; and (d) $t = 240 \mu\text{s}$.

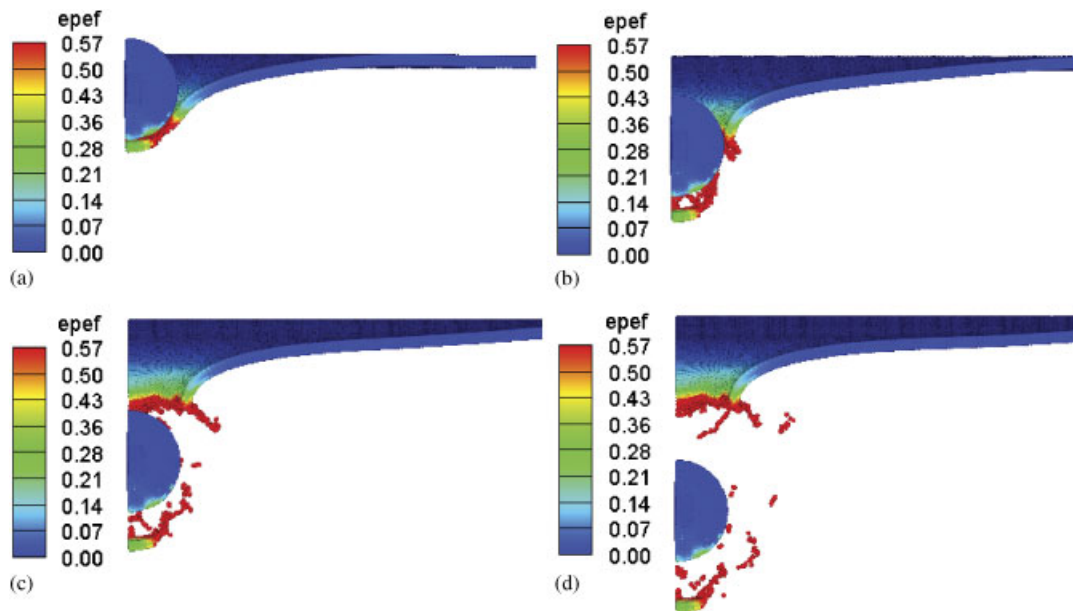


Figure 9. The configurations at various time step obtained by the second contact method, where epef represents the equivalent plastic strain $V_t = 85.8 \text{ m/s}$: (a) $t = 60 \mu\text{s}$; (b) $t = 120 \mu\text{s}$; (c) $t = 180 \mu\text{s}$; and (d) $t = 240 \mu\text{s}$.

Figure 10 compares the final deformed target plate obtained from the experiment [38] and simulations. In Figure 10, h is the height of the final deformed plate and D is the diameter of penetrated hole. The value of h/D obtained in the experiment is 0.84, and those obtained from

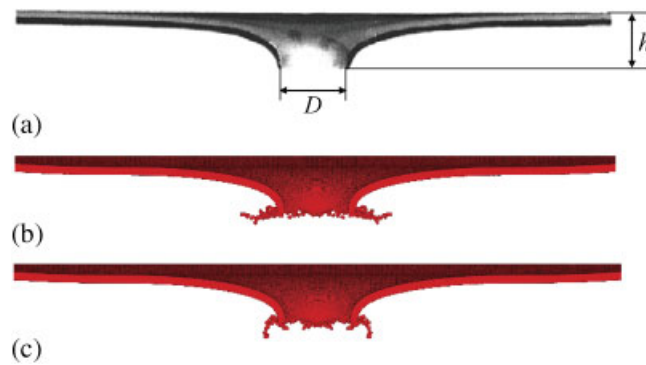


Figure 10. Final deformed shape of the target plate: (a) experimental graph; (b) obtained by the first contact method; and (c) obtained by the second contact method.

Table II. Effect of grid cell size on the simulation results.

Model	Dcell (mm)	Dp (mm)	Particles per cell	1st contact method		2nd contact method	
				V_r (m/s)	h/D	V_r (m/s)	h/D
M1	0.66	0.33	8	50.4	0.99	72.6	0.94
M2	0.60	0.20	27	70.6	0.88	74.0	0.87
M3	0.50	0.25	8	89.4	0.85	85.8	0.86
Experiment	—	—	—	—	0.84	—	0.84

the two contact methods are 0.85 and 0.86, respectively. The final deformed target plate obtained by the contact methods appears to be consistent with the experimental result.

The constitutive model used in this section is a local one in nature, without considering the plastic strain gradient. The computational results are affected by the cell size of background grid. To investigate the effect of the cell size and particle space on computational results, a convergence analysis is conducted using three models with different cell sizes and particle spaces, and numerical results are listed in Table II, in which Dcell represents the cell size and Dp represents the initial particle space. The projectile's residual velocity V_r increases and the target shape parameter h/D approaches the experimental result with the decrease of the cell size and particle space. The final deformed target obtained by M3 model is showed in Figure 10.

5.4. Perforation of thick plate

The final example is the impact of an ogive-nose high strength steel projectile against an aluminum target [41]. The projectile impacts a target obliquely with an angle of 30° . The projectile has a length of 88.9 mm and a diameter of 12.9 mm with a 3.0 caliber-radius-head. The target is an A6061-T651 plate of 26.3-mm thickness.

The projectile is modeled as an elastic material with the Young's modulus $E = 200$ GPa, the Poisson ratio $\nu = 0.3$ and the mass density $\rho = 7.85$ g/cm³. The target is modeled as an elastic-plastic material, whose deviatoric stress is updated using the Johnson Cook constitutive model

$$\sigma_y = (A + B\bar{\epsilon}_p^n)(1 + C \ln \dot{\epsilon}^*)(1 - T^{*m}) \quad (39)$$

where A , B , C , n and m are the material constants, $\dot{\epsilon}^*$ is the effective plastic strain rate and T^* is the dimensionless temperature. The pressure of target material is updated by the Mie-Grüneisen equation of state. The material constants for A6061-T651 are obtained from References [41] and [42], which are listed in Table III. When the effective plastic strain of a particle reaches the failure strain ϵ_{fail} , its deviatoric stress is set to zero.

Table III. Material constants of A6061-T651.

ρ (kg/m ³)	E (GPa)	μ	A (MPa)	B (MPa)	n	C	m	$\varepsilon_{\text{fail}}$
2700	69	0.3	262	52.1	0.41	0	0.859	1.6
c_0 (m/s)	s	γ_0	T_{melt} (K)	T_{room} (K)				
5350	1.34	2.0	875	293				

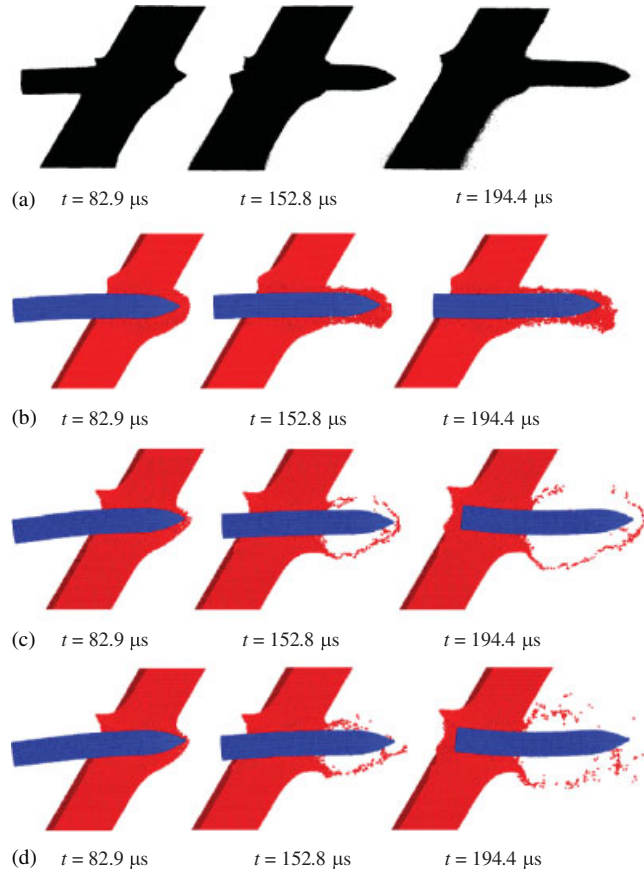


Figure 11. Projectile–target interaction at a striking velocity of $V_0=575$ m/s. V_r represents the projectile’s residual velocity: (a) experimental photographs, $V_r=455$ m/s; (b) simulation of the standard MPM, $V_r=334.1$ m/s; (c) simulation of the first contact MPM, $V_r=442.8$ m/s; and (d) simulation of the second contact MPM, $V_r=453.4$ m/s.

One half of the model is analyzed due to symmetry. The projectile is modeled with 13 314 particles, and the target is modeled with 187 550 particles. The cell size is set to 2.0 mm. The projectile has an initial particle space range from 0.6 to 1.0 mm, whereas the target has an initial particle space of 1.0 mm and eight material points per cell. The frictional coefficient μ between the projectile and the target is set to zero.

Figure 11 shows the projectile–target interaction in the experiment and simulation at a striking velocity of $V_0=575$ m/s. Figure 11(a) shows a sequence of X-ray photographs from experiments at different post impact times. The projectile’s residual velocity V_r in the experiment is 455 m/s. Figure 11(b) shows the projectile–target interaction in the standard MPM simulation. The projectile’s residual velocity V_r by the standard MPM simulation is 334.1 m/s, which is significantly lower than the experimental data of 455 m/s. MPM simulations with the contact methods are shown in Figures 11(c) and (d), respectively. The projectile’s residual velocities obtained by two

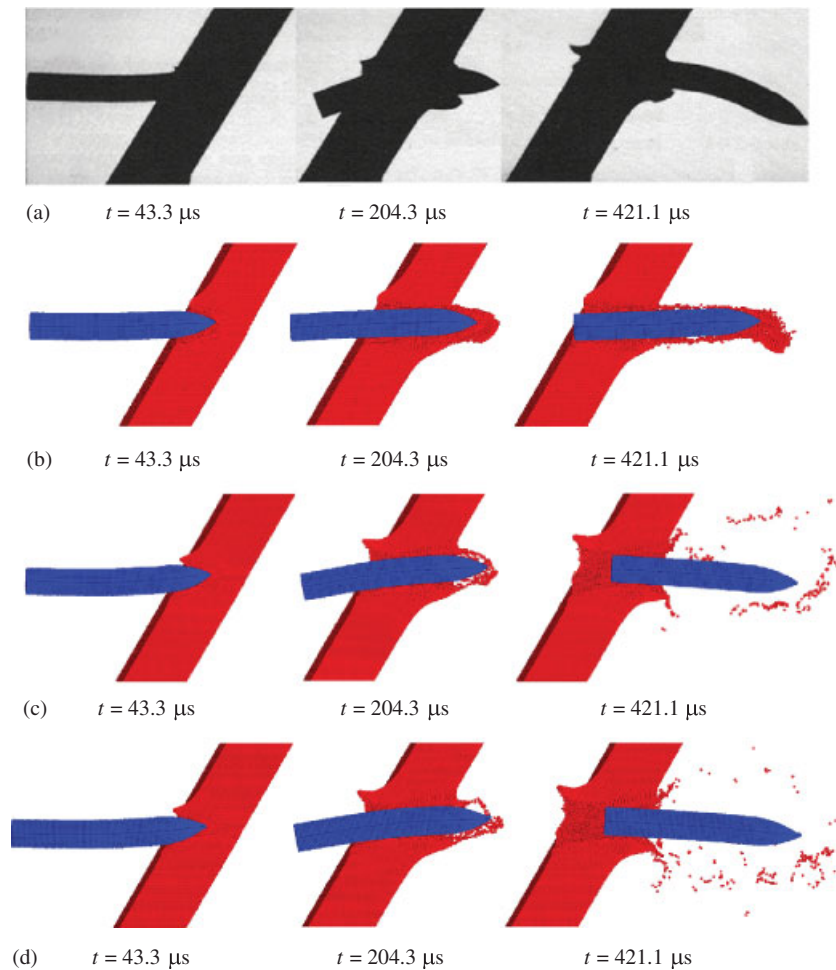


Figure 12. Projectile-target interaction at the striking velocity $V_0=400$ m/s. V_r represents the projectile's residual velocity: (a) experimental photographs, $V_r=217$ m/s; (b) simulation of the standard MPM, $V_r=127.9$ m/s; (c) simulation of the first contact MPM, $V_r=207.8$ m/s; and (d) simulation of the second contact MPM, $V_r=220.4$ m/s.

contact algorithms are 442.8 and 453.4 m/s, respectively, which agree well with that obtained by experiments. The CPU time for the simulation is about 173 min on a PC with Intel E7200 CPU (2.52 GHz) and 2 GB memory.

The residual velocity and the deformed shape of projectile are dependent on the striking velocity V_0 . Figure 12 shows the results of the experiment and simulation at the striking velocity $V_0=400$ m/s. Figure 12(a) shows the experimental photographs at different post impact times, and the projectile's residual velocity V_r in the experiment is 217 m/s. Figure 12(b) shows the projectile-target interaction in the standard MPM simulation, and V_r is 127.9 m/s. MPM simulations with the contact methods give more reasonable results, as shown in Figures 12(c) and (d). The projectile's residual velocities obtained by two contact algorithms are 207.8 and 220.4 m/s, respectively. Figure 12(a) shows that the steel projectile of the experiment is severely bent and yawed at $V_0=400$ m/s. The projectile's shape obtained by the contact methods (Figures 12(c) and (d)) is bent, whereas the projectile's shape obtained by the standard MPM (Figure 12(b)) is visibly undeformed at $V_0=400$ m/s. The projectile's shapes obtained by the contact methods appear to be more consistent with the experimental data than the standard MPM.

The penetrations of projectile with different striking velocities V_0 are simulated by using different MPM algorithms, and the projectile's residual velocities V_r are compared with the experimental

Table IV. The projectile's residual velocities for different striking velocities (m/s).

V_0	Experiment	Standard MPM	1st contact MPM	2nd contact MPM
340	91.0	0.0	83.8	96.5
400	217.0	127.9	207.8	220.4
446	288.0	197.5	280.0	291.1
575	455.0	334.1	442.8	453.4
730	655.0	478.4	623.9	634.5

results in Table IV. The projectile's residual velocities obtained by the standard MPM are significantly less than the experiment results, whereas the results obtained by proposed contact methods are in good agreement with the experimental results. The inherent no-slip contact condition in the standard MPM creates a greater penetration resistance, so that the target absorbs more impact energy and decreases the projectile's residual velocity significantly. In contrast, MPM simulations with contact methods give more reasonable results.

6. CONCLUSIONS

Two contact methods are presented for MPM in impact and penetration simulation. Numerical studies show that the first contact method introduces significant disturbance into the total energy in the collision of two elastic rings due to the violation of the impenetrability condition in updating stresses on particles, and the second method can achieve stable solution by using much larger time step than the first contact method. However, it seems that both contact methods give good results for other problems, such as the sphere rolls and slips on a inclined plane, in which the velocity is low so that the magnitude of the discontinuities of normal velocities at contacted nodes on the redefined regular grid is small.

In the penetration simulations, the inherent no-slip contact condition in the standard MPM creates a great penetration resistance, so that the target absorbs more impact energy and decreases the projectile velocity. The projectile's residual velocity obtained by the standard MPM simulation is significantly lower than the experimental data. Numerical studies show that the projectile's residual velocities obtained by the proposed contact methods are higher than those obtained by the standard MPM method, and are closer to the experimental results.

ACKNOWLEDGEMENTS

This work is supported by the National Basic Research Program of China (2010CB832701) and National Natural Science Foundation of China (10872107). The authors thank Dr Xiaofei Pan of Institute of Applied Physics and Computational Mathematics of Beijing for his helpful discussions of contact algorithms. Thanks go to Dr Xiaowei Chen of China Academy of Engineering Physics (CAEP) for his suggestions of numerical examples. Thanks also to Dr Gang Chen of CAEP for his helpful discussions of material constitutive models.

REFERENCES

1. Anderson Jr CE, Bodher SR. Ballistic impact: the status of analytical and numerical modeling. *International Journal of Impact Engineering* 1988; **7**:9–35.
2. Benson DJ. Computational methods in Lagrangian and Eulerian hydrocodes. *Computer Methods in Applied Mechanics Engineering* 1992; **99**:235–394.
3. Silling SA. Eulerian simulation of the perforation of aluminum plates by nondeforming projectiles. *Technical Report SAND92-0493*, Sandia National Laboratories, Albuquerque, NM, 1992.
4. Scheffler DR. Modeling non-eroding perforation of an oblique aluminum target using the Eulerian CTH hydrocode. *International Journal of Impact Engineering* 2005; **32**:461–472.
5. Camacho GT, Ortiz M. Computational modeling of impact damage in brittle materials. *International Journal of Solids and Structures* 1996; **33**:2899–2938.

6. Camacho GT, Ortiz M. Adaptive Lagrangian modeling of ballistic penetration of metallic targets. *Computer Methods in Applied Mechanics Engineering* 1997; **142**:269–301.
7. Liu WK, Belytschko T, Chang H. An arbitrary Lagrangian–Eulerian finite element method for path-dependent materials. *Computer Methods in Applied Mechanics Engineering* 1986; **58**:227–245.
8. Johnson GR, Stryk RA, Beissel SR. SPH for high velocity impact computations. *Computer Methods in Applied Mechanics Engineering* 1996; **139**:347–373.
9. Han ZD, Liu HT, Rajendran AM, Atluri SN. The applications of meshless local Petrov–Galerkin (MLPG) approaches in high-speed impact, penetration and perforation problems. *CMES: Computer Modeling in Engineering and Sciences* 2006; **14**:119–128.
10. Sulsky D, Chen Z, Schreyer H. A particle method for history-dependent materials. *Computer Methods in Applied Mechanics Engineering* 1994; **118**:179–196.
11. Sulsky D, Zhou S, Schreyer H. Application of a particle-in-cell method to solid mechanics. *Computer Physics Communications* 1995; **87**:236–252.
12. Harlow FH. The particle-in-cell computing method for fluid dynamics. *Methods in Computational Physics* 1963; **3**:319–343.
13. Brackbill JU, Kothe DB, Ruppel HM. FLIP: a low-dissipation, particle-in-cell method for fluid flow. *Computer Physics Communications* 1988; **48**:25–38.
14. Sulsky D, Kaul A. Implicit dynamics in the material-point method. *Computer Methods in Applied Mechanics and Engineering* 2004; **193**:1137–1170.
15. Sulsky D, Schreyer HL. Axisymmetric form of the material point method with applications to upsetting and Taylor impact problems. *Computer Methods in Applied Mechanics Engineering* 1996; **139**:409–429.
16. Guo Y, Nairn JA. Three-dimensional dynamic fracture analysis using the material point method. *Computer Modeling in Engineering and Sciences* 2006; **16**:141–156.
17. Tan HL, Nairn JA. Hierarchical, adaptive, material point method for dynamic energy release rate calculations. *Computer Methods in Applied Mechanics and Engineering* 2002; **191**:2095–2109.
18. Hu W, Chen Z. Model-based simulation of the synergistic effects of blast and fragmentation on a concrete wall using the MPM. *International Journal of Impact Engineering* 2006; **32**:2066–2096.
19. Guilkey JE, Harman TB, Banerjee B. An Eulerian–Lagrangian approach for simulating explosions of energetic devices. *Computers and Structures* 2007; **85**:660–674.
20. Zhang X, Sze KY, Ma S. An explicit material point finite element method for hyper-velocity impact. *International Journal for Numerical Methods in Engineering* 2006; **66**:689–706.
21. Ma S, Zhang X, Qiu XM. Comparison study of MPM and SPH in modeling hypervelocity impact problems. *International Journal of Impact Engineering* 2009; **36**:272–282.
22. Zhang HW, Wang KP. *et al.* Material point method for dynamic analysis of saturated porous media under external contact/impact of solid bodies. *Computer Methods in Applied Mechanics and Engineering* 2009; **198**(17–20):1456–1472.
23. York AR II, Sulsky D, Schreyer HL. The material point method for simulation of thin membranes. *International Journal for Numerical Methods in Engineering* 1999; **44**:1429–1456.
24. Hu W, Chen Z. A multi-mesh MPM for simulating the meshing process of spur gears. *Computers and Structures* 2003; **81**:1991–2002.
25. Bardenhagen SG, Brackbill JU, Sulsky D. The material point method for granular materials. *Computer Methods in Applied Mechanics Engineering* 2000; **187**:529–541.
26. Bardenhagen SG, Guilkey JE, Roessig KM, Brackbill JU, Witzel WM, Foster JC. An improved contact algorithm for the material point method and application to stress propagation in granular material. *Computer Modeling in Engineering and Sciences* 2001; **2**(4):509–522.
27. Pan XF, Xu AG, Zhang GC *et al.* Three-dimensional multi-mesh material point method for solving collision problems. *Communications in Theoretical Physics* 2008; **49**:1129–1138.
28. Bardenhagen SG. Energy conservation error in the material point method for solid mechanics. *Journal of Computational Physics* 2002; **180**:383–403.
29. Nairn JA. Material point method calculations with explicit cracks. *Computer Modeling in Engineering and Sciences* 2003; **4**(6):649–663.
30. Chen Z, Brannon R. An evaluation of the material point method. *Technical Report SAND 2002-0482*, Sandia National Laboratories, Albuquerque, NM, 2002.
31. Bardenhagen SG, Brackbill JU. Dynamic stress bridging in granular material. *Journal of Applied Physics* 1998; **83**:5732–5740.
32. Wang FJ, Wang LP, Cheng JG, Yao ZH. Contact force algorithm in explicit transient analysis using finite-element method. *Finite Elements in Analysis and Design* 2007; **43**:580–587.
33. Belytschko T, Neal MO. Contact-impact by the pinball algorithm with penalty and Lagrangian methods. *International Journal for Numerical Methods in Engineering* 1991; **131**:547–572.
34. Cummins SJ, Brackbill JU. An implicit particle-in-cell method for granular materials. *Journal of Computational Physics* 2002; **180**:506–548.
35. Belytschko T, Liu WK, Moran B. *Nonlinear Finite Element for Continua and Structures*. Wiley: New York, 2000.
36. Gray JP, Monaghan JJ, Swift RP. SPH elastic dynamics. *Computer Methods in Applied Mechanics Engineering* 2001; **190**:6641–6662.

37. Monaghan JJ. SPH without a tension instability. *Journal of Computational Physics* 2000; **159**:290–311.
38. Seoa SW, Min OK, Lee JH. Application of an improved contact algorithm for penetration analysis in SPH. *International Journal of Impact Engineering* 2008; **35**:578–588.
39. De Vuyst T, Vignjevic R, Campbell JC. Coupling between meshless and finite element methods. *International Journal of Impact Engineering* 2005; **31**:1054–1064.
40. Wingate CA, Dilts GA, Mandell DA, Crotzer LA, Knapp CE. Progress in smooth particle hydrodynamics. *Technical Report LA-UR-98-300*, Los Alamos National Laboratories, Los Alamos, NM, 1998.
41. Piekutowski AJ, Forrestal MJ, Poormon KL, Warren TL. Perforation of aluminium plates with ogive-nose steel rods at normal and oblique impacts. *International Journal of Impact Engineering* 1996; **18**:877–887.
42. Meyers MA. *Dynamics Behavior of Materials*. Wiley: New York, 1994.